



Improving Planet Detection with Disk Modeling: Keck/NIRC2 Imaging of the HD 34282 Single-armed Protoplanetary Disk

Juan Quiroz¹ , Nicole L. Wallack² , Bin Ren (任彬)^{1,6} , Ruobing Dong (董若冰)³ , Jerry W. Xuan¹ , Dimitri Mawet^{1,4} , Maxwell A. Millar-Blanchaer⁵ , and Garreth Ruane⁴

¹ Department of Astronomy, California Institute of Technology, MC 249-17, 1200 East California Boulevard, Pasadena, CA 91125, USA; ren@caltech.edu

² Division of Geological & Planetary Sciences, California Institute of Technology, MC 170-25, 1200 East California Boulevard, Pasadena, CA 91125, USA
nwallack@caltech.edu

³ Department of Physics & Astronomy, University of Victoria, Victoria, BC, V8P 1A1, Canada

⁴ Jet Propulsion Laboratory, California Institute of Technology, 4800 Oak Grove Drive, Pasadena, CA 91109, USA

⁵ Department of Physics, University of California, Santa Barbara, CA 93106, USA

Received 2021 October 4; revised 2021 November 23; accepted 2021 November 24; published 2022 January 4

Abstract

Formed in protoplanetary disks around young stars, giant planets can leave observational features such as spirals and gaps in their natal disks through planet–disk interactions. Although such features can indicate the existence of giant planets, protoplanetary disk signals can overwhelm the innate luminosity of planets. Therefore, in order to image planets that are embedded in disks, it is necessary to remove the contamination from the disks to reveal the planets possibly hiding within their natal environments. We observe and directly model the detected disk in the Keck/NIRC2 vortex coronagraph L' -band observations of the single-armed protoplanetary disk around HD 34282. Despite a nondetection of companions for HD 34282, this direct disk modeling improves planet detection sensitivity by up to a factor of 2 in flux ratio and $\sim 10 M_{\text{Jupiter}}$ in mass. This suggests that performing disk modeling can improve directly imaged planet detection limits in systems with visible scattered light disks, and can help to better constrain the occurrence rates of self-luminous planets in these systems.

Unified Astronomy Thesaurus concepts: [Protoplanetary disks \(1300\)](#); [Coronagraphic imaging \(313\)](#); [Planetary system formation \(1257\)](#)

Supporting material: data behind figure

1. Introduction

The most recent generation of high-contrast imaging surveys that utilize extreme adaptive optics systems have obtained an occurrence rate of $\lesssim 10\%$ for young self-luminous giant planets (i.e., Nielsen et al. 2019; Vigan et al. 2021). Despite their low direct occurrence rates using contemporary instruments, giant planets can gravitationally interact with their surrounding gaseous protoplanetary disks and leave their mark as observational signatures in the disk structure (e.g., spirals, gaps; Dong et al. 2015b, 2015c; Bae et al. 2018). Therefore, protoplanetary disks with suspected embedded forming planets not only are excellent targets for giant planet detection (e.g., Haffert et al. 2019; Wang et al. 2020), but also can help constrain planet–disk interactions (e.g., Bae et al. 2019; Rosotti et al. 2020).

While protoplanetary disks with planet–disk interaction signatures may be prime targets for observing actively forming planets, they can also hinder the detection of planets (see Kepler et al. 2018; Wang et al. 2020). Specifically, using the current prevailing observation and data reduction strategy for ground-based high-contrast imaging (i.e., angular differential imaging, or ADI; Marois et al. 2006), disk signals can remain in the reduced images and overwhelm planetary signals, resulting in lower sensitivity to detecting planets in the regions where disk signals dominate (e.g., Figure 12 of Maire et al. 2017, Figure 6

of de Boer et al. 2021, Figure 4 of Asensio-Torres et al. 2021). Moreover, even after processing, disk signals can mimic the appearances of protoplanets (e.g., HD 100546: Quanz et al. 2013; Currie et al. 2014; HD 169142: Biller et al. 2014; Reggiani et al. 2014), making it challenging to distinguish planets from disk features. Indeed, it is only after modeling and removing the disk from the PDS 70 system that Wang et al. (2020) could recover the disk-embedded protoplanet PDS 70 c. Therefore, in addition to utilizing diverse approaches in both observation and data reduction methods, it is necessary to investigate whether disk modeling could also improve our sensitivity to planets detected via ground-based high-contrast imaging, which could possibly lead to more detections in blind-search surveys.

Although spirals and rings are indications of the existence of planets, they can also possibly result from mechanisms that do not involve planets (e.g., spirals: Dong et al. 2015a; Montesinos & Cuello 2018; Hall et al. 2020, gaps: Birnstiel et al. 2015; van der Marel et al. 2018). Although the formation of spirals in protoplanetary disks can be caused both with and without planets, the differing mechanisms may be distinguishable via the structure in the disk. For example, gravitational-instability-triggered spiral arms are likely symmetric and have even-numbered spirals (e.g., Dong et al. 2015a), whereas planet-induced spirals can be less symmetric. Another reason to search spiral disks for planet signals is that gap-opening planets (e.g., Zhang et al. 2018; Lodato et al. 2019) could be less massive than spiral-arm-driving planets (e.g., Figure 1 of Bae et al. 2018), and most gap-opening planets are beyond the detection limits of current instruments. Therefore, in order to have the best chance of detecting a massive companion, herein

⁶ To whom correspondence should be addressed.

we focus on planet detection in the single spiral-arm system HD 34282 (de Boer et al. 2021), specifically focusing on improving planetary detection limits by modeling the observed disk structure.

Located at 309 ± 2 pc (Gaia Collaboration et al. 2021), HD 34282 is an A3V star (Merín et al. 2004) with a protoplanetary disk containing a 75 au cavity⁷ in 0.87 mm ALMA continuum emission observations (van der Plas et al. 2017). With an overdensity in the southeast region of its ALMA-detected ring (which has an inclination of $59^\circ 3 \pm 0^\circ 4$ and a position angle of $117^\circ 1 \pm 0^\circ 3$), van der Plas et al. (2017) suggested that a $\approx 50 M_{\text{Jupiter}}$ brown dwarf companion at $\approx 0'' 1$ could be responsible for shepherding the dust in the HD 34282 system, favoring this explanation over a nonplanet-driven photoevaporation mechanism for opening the cavity. In *J*-band polarized light observations using VLT/SPHERE, de Boer et al. (2021) identified two rings with a $\sim 56^\circ$ inclination and a $\sim 119^\circ$ position angle, and a possible tightly wound single-arm spiral that resembles the pattern driven by a sub-Jupiter- to Jupiter-mass planet (e.g., Dong et al. 2015c; Dong & Fung 2017). However, the observations in de Boer et al. (2021) were not sensitive enough to detect a planet of such mass. Moreover, the planet-detection map in Figure 6 of de Boer et al. (2021) is affected by the signal of the disk, which causes the sensitivity to drop from $\lesssim 4 M_{\text{Jupiter}}$ in exterior regions of the image to $\gtrsim 10 M_{\text{Jupiter}}$ in the regions hosting disk signals.

Herein we present *L'*-band imaging of the HD 34282 system using the Keck/NIRC2 vortex coronagraph. Motivated by the recovery of the PDS 70 c planet via disk modeling in Wang et al. (2020), we investigate the effect of disk modeling in planet detection using HD 34282. Specifically, we model the observed NIRC2 disk as an experiment in a targeted search for planets that are embedded in disks. We describe the NIRC2 observations in Section 2, we present the observed features and investigate the effects of disk modeling in Section 3, and we summarize our findings in Section 4.

2. Observation and Data Reduction

We observed HD 34282 using Keck/NIRC2 in *L'*-band (central wavelength: $3.8 \mu\text{m}$) under program C328 (PI: G. Ruane) on UT 2017 February 07 from 04:43 to 07:15. We use the narrow camera which has a pixel size of 9.942 mas and a 1024×1024 pixel field of view (i.e., $10'' 18 \times 10'' 18$). With 73 science frames covering a parallactic angle change of $61^\circ 3$, where each frame consists of 45 coadds with 1 s exposures, we have a total integration time of 3285 s on HD 34282. During the observation, the coherence time was $\tau_0 \approx 0.87$ ms at $0.5 \mu\text{m}$ (Xuan et al. 2018), the WRF seeing⁸ was between $1'' 32$ and $1'' 45$, and the airmass was 1.19 ± 0.05 . We preprocess the data using the VIP (Gomez Gonzalez et al. 2017) package that is customized for NIRC2 vortex observations by performing flat-fielding, background removal, and image centering. By comparing the central pixels between the output point-spread function (PSF) and an ideal model, the Strehl ratio was between 0.63 and 0.66 for this observation. See Xuan et al. (2018) for a description of both the pipeline that utilizes the VIP package and a thorough characterization of the Keck/NIRC2 vortex coronagraph.

To reveal the extent of the disk while maximizing computational efficiency, we crop each preprocessed image to a 201×201 pixel field while discarding the last 4 exposures due to poor image quality. In the following analysis, we focus on an annular region that is between 20 pixels and 100 pixels from the star. To extract the HD 34282 system from the raw observations, we first capture the speckle features using the principal-component-analysis-based Karhunen–Loève image projection (KLIP; Soummer et al. 2012) method implemented in the `DebrisDiskFM` package (Ren et al. 2019). To balance speckle removal and ADI self-subtraction, with the former requiring more and the latter requiring fewer KLIP components in data reduction, we use the first 6 KLIP components to remove speckles while preserving the morphology of the disk. We rotate each of the reduced 69 images to north–up and east–left, then calculate their mean to obtain the final image for the HD 34282 system, shown in Figure 1(a).

We also acquire the de Boer et al. (2021) *J*-band observations of HD 34282 in polarized light from UT 2015 December 19 using SPHERE/IRDIS (e.g., de Boer et al. 2020) under European Southern Observatory (ESO) program 096.C-0248(A) (PI: J.-L. Beuzit) from the ESO Science Archive Facility. To reveal the extent of the disk, we use `IRDAP` which performs polarimetric differential imaging (PDI) from van Holstein et al. (2020) to reduce the IRDIS observations. In Figures 1(b) and (c), we show the SPHERE Q_ϕ map and overlay the SPHERE contours (the contour levels are selected to match features in both data sets) on our NIRC2 data.

3. Analysis

3.1. Disk Features

The ADI image of HD 34282 in the NIRC2 *L'*-band is composed of a ring and a blob in the northwest direction (shown in Figure 1(a)). The ring extends to $\approx 0'' 5$, and its southeast half is brighter than the northwest half by $\approx 40\%$. The northwest blob is located outside the inner working angle of $0'' 2$ at a position angle of -60° east of north.

The northwest NIRC2 blob is not a planetary signal. Compared with the SPHERE PDI data in Figure 1(c), it is the inner ring component “R2” identified in de Boer et al. (2021). However, we do not recover the southeast side of R2 in our NIRC2 observations; this could be explained by self-subtraction effects with ADI using KLIP. Either reference-star differential imaging (e.g., Ruane et al. 2019), or advanced ADI speckle-removal methods (e.g., Ren et al. 2020; Flasseur et al. 2021; Pairet et al. 2021) are needed to recover the whole extent of R2.

The NIRC2 ring, which has an apparent brightness asymmetry, is in fact composed of multiple features identified in the SPHERE data in de Boer et al. (2021). Specifically, the southeast half of the NIRC2 ring is a superposition of the SPHERE arm and outer ring, or the “B1” and “R1” features in de Boer et al. (2021), respectively. As evident in the SPHERE data, the southeast half of R1 is fainter than B1, causing B1 to dominate the signal in our NIRC2 data.

3.2. Disk Forward Modeling

Observing an apparent ring-like structure in our *L'*-band data in Figure 1(a), we use the Millar-Blanchaer et al. (2015) code⁹ to model the system with a ring. To take into account the observed apparent brightness asymmetry of HD 34282 evident

⁷ Size scaled to match Gaia Collaboration et al. (2021) distance.

⁸ <http://mkwc.ifa.hawaii.edu/current/seeing/index.cgi>

⁹ https://github.com/maxwellmb/anadisk_model

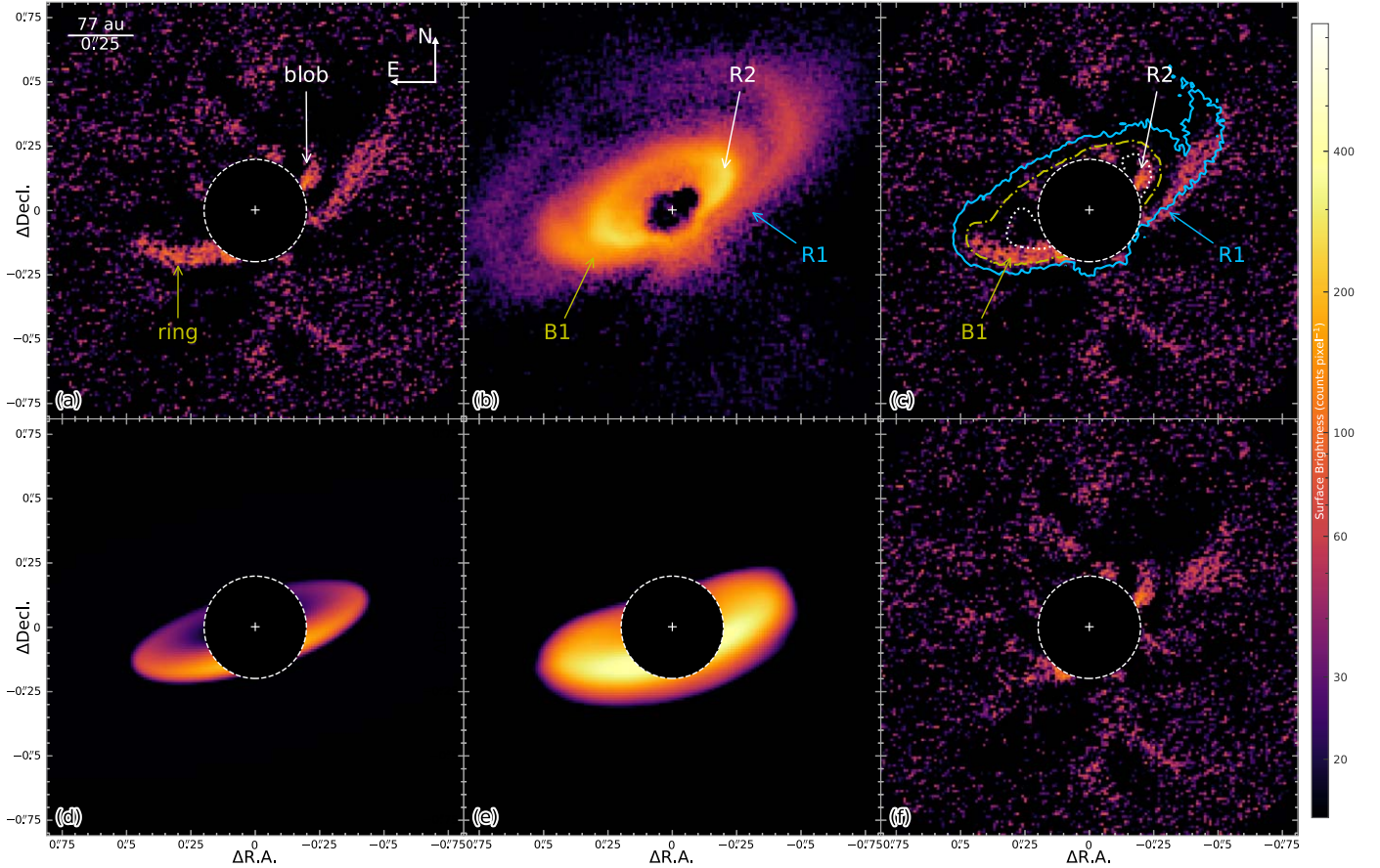


Figure 1. Keck/NIRC2 imaging and modeling of the HD 34282 system in the L' -band. (a) Reduction result of the original exposures. (b) SPHERE Q_ϕ image, following annotations in Figure 2 of de Boer et al. (2021). (c) SPHERE contours overlaid on the NIRC2 image: we confirm the existence of the B1 spiral. (d) Best-fit disk model for the NIRC2 ring. (e) Best-fit disk model with instrumentation effects taken into account (i.e., convolution, transmission) for a representative one of the 69 exposures: the actual convolution is performed for all of the exposures. (f) Reduction residuals after removing the best-fit instrumental disk model from the original exposures. Note: the images are shown in log scale, the dashed central region with a 20 pixel radius is masked out in our data analysis; and the SPHERE data have different display limits than the NIRC2 data.

(The data used to create this figure are available.)

in both the SPHERE data presented in de Boer et al. (2021) and our NIRC2 data, we use the function in the updated code which can offset the ring from the assumed central star location (presented in Millar-Blanchaer et al. 2016). We aim to reproduce the observed ring using geometric models to investigate the effect of disk modeling on planet detection; therefore, we assume the disk is optically thin for simplicity. Thus, we do not focus on retrieving physical parameters for the observed HD 34282 ring or on the physical meaning of the ring-center offset from the star (e.g., Table 1 of de Boer et al. 2021). We acknowledge that such a disk model is not physically motivated, especially after the polarized light observations in de Boer et al. (2021); therefore, we only focus on the visible structure seen in the NIRC2 L' data and not on its physical origins.

We use the Ren et al. (2021) modification of the Millar-Blanchaer et al. (2015) code, which describes the ring with a double power law (Augereau et al. 1999) along the midplane and a Gaussian dispersion along the vertical axis:

$$\rho(r, z) \propto \left[\left(\frac{r}{r_c} \right)^{-2\alpha_{\text{in}}} + \left(\frac{r}{r_c} \right)^{-2\alpha_{\text{out}}} \right]^{-\frac{1}{2}} \exp \left[-\left(\frac{z}{hr} \right)^2 \right], \quad (1)$$

where r_c is the critical radius, α_{in} and α_{out} are the asymptotic power-law indices interior and exterior to r_c , and h is the scale height. We use the `DebrisDiskFM` framework by Ren et al. (2019) to explore disk parameters using `emcee` (Foreman-Mackey et al. 2013). Specifically, we perform forward modeling to minimize the residuals in our reduction. We first generate a ring model using the Millar-Blanchaer et al. (2015) code assuming given ring parameters (i.e., inclination, position angle, brightness, ring-center offsets along the apparent major and minor axes, critical radius, and power-law indices) and forward-scattering coefficient of the dust particles (i.e., Henyey & Greenstein 1941). We then simulate the NIRC2 instrument response on the disk model by rotating the model according to the parallactic angles for each of the 69 exposures, convolving with the PSF, and multiplying the result by the transmission map of the NIRC2 vortex coronagraph.

To obtain the best-fit disk model for the observed disk structure, we note that disk signals are overfit by speckle features using KLIP (Pueyo 2016); we thus perform forward modeling using negative injection of the disk signals to minimize the residuals. Specifically, we remove the instrument's response to the disk models from the original exposures and perform KLIP ADI reduction using 6

components (i.e., identical KLIP parameters to the original data reduction in Section 2). The best-fit model is the one that minimizes the chi-squared residuals. We list in the Appendix the best-fit parameters, with their uncertainties derived assuming the pixels are mutually independent. By focusing on the ring regions, we obtain the best-fit disk model shown in Figure 1(d), and the corresponding residual map presented in Figure 1(f).

Due to the existence of the ring brightness asymmetry in the NIRC2 data and the two-ringed architecture in the SPHERE data, we have performed additional model fitting not shown in Figure 1. We have attempted to fit the two halves (i.e., northwest and southeast) of the NIRC2 ring with two half-rings, both centered on the star. The preferred two half-ring models drift toward nearly edge-on, inconsistent with observations of this system, which suggests they are likely offset from the star. We have also tried to fit the northwest blob in the NIRC2 data with a smaller ring, as motivated by the existence of R2 in the SPHERE observations. We cannot find a model that fits this structure since such a ring requires a counterpart in the southeast (e.g., Figure 1(c)), which is missing in the NIRC2 observations. We thus adopt an offset ring to describe the NIRC2 data to minimize the number of free parameters in our model.

3.3. L' -band Magnitude of HD 34282

The WISE $W1$ band covers a portion of the Keck/NIRC2 L' -band wavelengths, we thus use the former to obtain the L' magnitude for HD 34282. We first generate a high-resolution stellar spectrum by interpolating within the PHOENIX stellar model grid from Husser et al. (2013) to match the stellar parameters from Merín et al. (2004). In order to match the model spectrum to the observed WISE $W1$ value of 7.072 ± 0.016 (CatWISE2020; Marocco et al. 2021), we scale the resulting model flux when integrated across the $W1$ bandpass (Rodrigo et al. 2012; Rodrigo & Solano 2020). We then take the resulting scaled spectrum, account for the transmission through the atmosphere, and integrate across the Keck/NIRC2 L' filter profile (Rodrigo et al. 2012; Rodrigo & Solano 2020) to obtain an L' magnitude of $7.729^{+0.015}_{-0.017}$.

3.4. Detection Limits

We obtain the detection sensitivity to planets by injecting point sources into the observations and calculating their signal-to-noise (S/N) values after KLIP ADI reduction. To investigate the effect of disk modeling on point-source detection, we calculate the contrast before and after removing the best-fit model in Figure 1(d) from the observations. We calculate 1D contrast curves with radial distance from the host star using VIP which utilizes fake companion injection and recovery when determining the contrast achieved at different radial distances. We compare the contrast achieved in the image where we remove the best-fitting disk to that in which we do not in Figure 2. Comparing the two contrast curves, we find a marked improvement in the contrast achieved at the radial separations where the disk is visible. We also test the effect of utilizing a high-pass filter (HPF) to remove the disk structure, which in essence is treating the disk as noise. We find that an improvement is seen for both the original data and the data in which we use an HPF.¹⁰

¹⁰ We smooth each raw exposure with a Gaussian that is two times the full width at half maximum of the PSF, and remove it from the raw exposure.

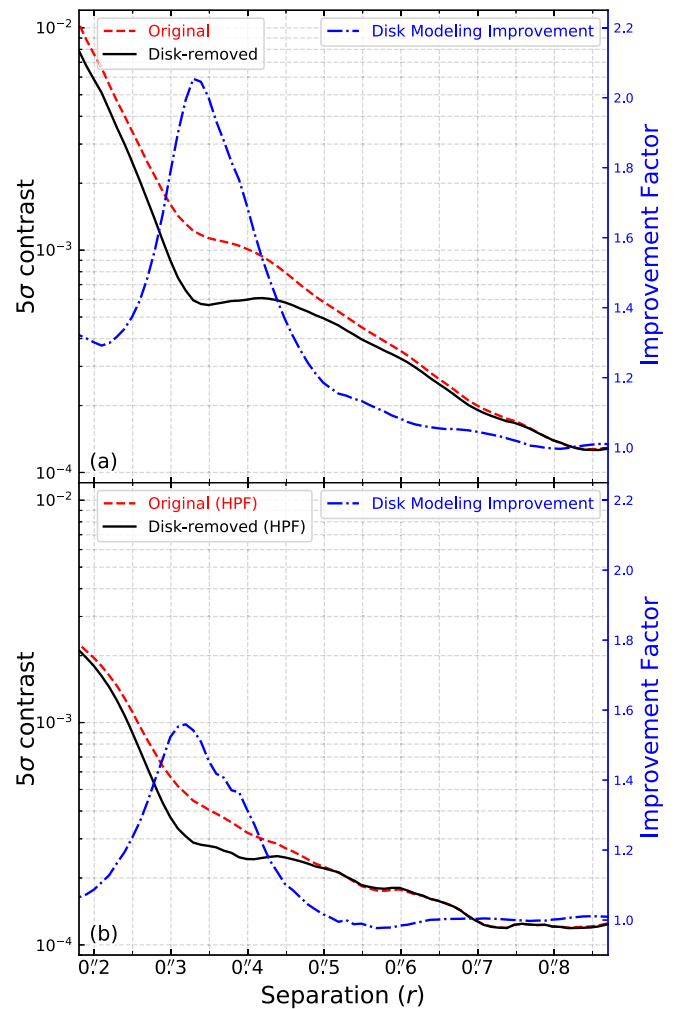


Figure 2. 5σ detection limit of point sources as a function of radial separation for our observations. The red dashed line is the contrast curve for the original data, and the black solid line is the contrast curve for the data with the best-fit disk model removed. By dividing the two contrast curves (see blue dashed-dotted line), we obtain a better overall detection limit. For the disk region, when removing the disk, we are more sensitive by a factor of ~ 2 over the original data in panel (a), and ~ 1.6 for the high-pass filtered data in panel (b).

While using an HPF allows us to achieve better contrast than not using an HPF, the data with the HPF does degrade the quality of the extended disk structure seen in this system; therefore, we focus on the data without the HPF in order to highlight the effect that disk modeling has. For the data without the HPF, we then utilize our 1D contrast curves and the AMES-Cond models (Baraffe et al. 2003) to determine what mass planets we are sensitive to with our improved contrast limits after removing the disk. The AMES-Cond evolutionary models predict how luminous an object will be given a mass and age. We use our L' stellar magnitude, our contrast limits, and the published age for this system ($6.4^{+1.9}_{-2.6}$ Myr; van der Plas et al. 2017) to determine expected mass limits in the disk plane based on disk parameters in van der Plas et al. (2017). We interpolate within the AMES-Cond model grid and determine the mass corresponding to our contrast with radial separation in Figure 3.

We can reach a typical sensitivity of $\sim 10 M_{\text{Jupiter}}$ assuming the AMES-Cond models. However, our sensitivity is sub-optimal in the region where the disk signal resides at ~ 200 au, as has been observed in Figure 6 of de Boer et al. (2021).

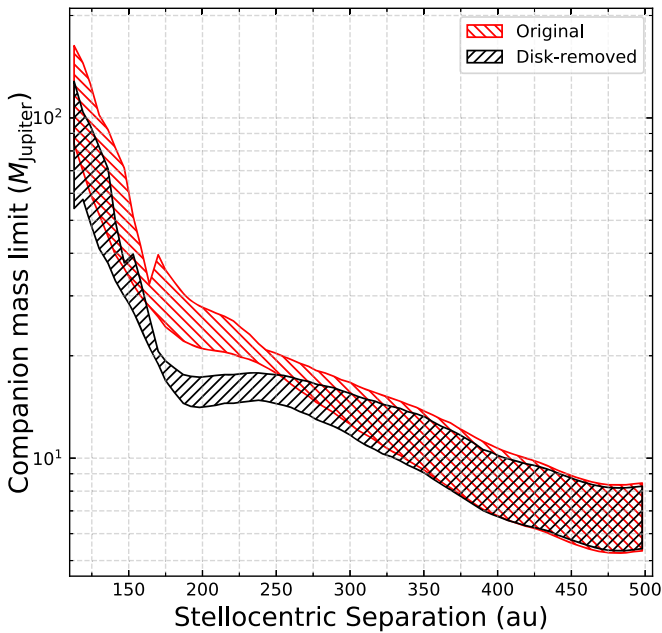


Figure 3. Mass limits using the AMES–Cond models for our observations with the disk present (in red) and after removing the disk (in black) as a function of separation in au (after accounting for the effects of an inclination-based projection). The width of the shaded regions account for uncertainties in the distance, age, and magnitude of the host star. We are sensitive to planets $\sim 10 M_{\text{Jupiter}}$ smaller after removing the best-fitting disk model in the region where the disk is present. Note: the minimum stellocentric separation presented here is outside the coronagraph to avoid possible coronagraphic occultation; future analysis at shorter separations should take the occultation probability into account.

Utilizing disk modeling, we are able to reach a sensitivity of $\sim 15 M_{\text{Jupiter}}$ at ~ 200 au, a factor of ~ 2 better in comparison to the original reduction. As a result, we are able to achieve better sensitivity by performing disk modeling, allowing us to be more sensitive to smaller planets, possibly allowing for better constraints on the occurrence rate of less massive planets.

4. Summary

We model the L' observation of the single-armed spiral disk HD 34282 using an offset geometric disk model. We show that even using a nonphysical simplified model allows for better achieved sensitivity over not modeling the disk. Therefore, we recommend modeling the disks in scattered light systems to increase the sensitivity to less massive planets. In fact, the importance of modeling observed disks is demonstrated in Wang et al. (2020), where the luminosity of PDS 70 c was only evident after disk modeling. In addition to the established two steps of planet imaging (instrumentation and observation design, and postprocessing for speckle noise removal), our study herein suggests that a third step is necessary in cases where we detect disks in scattered light—performing disk modeling to disentangle nonplanetary astrophysical signals to reveal possibly obscured planets.

We caution that for the purpose of targeted planet searches, one should mask out expected planet regions during the disk-modeling process as in Wang et al. (2020) for PDS 70 c. In our study of NIRC2 imaging of HD 34282, one additional caveat is that possible planets can be fit out by the offset ring model. Nevertheless, the simulations in Dong & Fung (2017) suggest that planets inducing a single spiral arm can be $0.1\text{--}1 M_{\text{Jupiter}}$. Such a planet is expected to be undetectable even after the

removal of the disk signal following the Wang et al. (2020) approach. Despite this, we note that a variation of the Wang et al. (2020) approach—specifically, masking out different regions while disk modeling for an exhaustive search of unknown planets—could still be necessary for other systems.

We also caution that physically motivated disk models satisfying dynamical constraints are preferred in order to characterize the scattered light signals while modeling. Our simple assumptions in the models presented herein show a first attempt at subtracting disk signals in order to improve planet-detection capabilities. Future studies, including those along the lines of, e.g., Wolff et al. (2017) and Villenave et al. (2019), to characterize the dust properties in the HD 34282 disk, are needed to refine the models.

We thank the anonymous referee for comments that improved this Letter. This research is partially supported by NASA ROSES XRP award 80NSSC19K0294. We thank Jean-Baptiste Ruffio, Jason Wang, Christian Ginski, and Myriam Benisty for discussions on calculating contrast curves. R. D. acknowledges financial support provided by the Natural Sciences and Engineering Research Council of Canada through a Discovery Grant as well as the Alfred P. Sloan Foundation through a Sloan Research Fellowship. Some of the data presented herein were obtained at the W. M. Keck Observatory, which is operated as a scientific partnership among the California Institute of Technology, the University of California, and the National Aeronautics and Space Administration. The Observatory was made possible by the generous financial support of the W. M. Keck Foundation. The authors wish to recognize and acknowledge the very significant cultural role and reverence that the summit of Maunakea has always had within the indigenous Hawaiian community. We are most fortunate to have the opportunity to conduct observations from this mountain. Part of the computations presented here were conducted in the Resnick High Performance Computing Center, a facility supported by the Resnick Sustainability Institute at the California Institute of Technology. Based on observations collected at the European Organisation for Astronomical Research in the Southern Hemisphere under ESO program 096.C-0248(A). This publication makes use of data products from the Wide-field Infrared Survey Explorer, which is a joint project of the University of California, Los Angeles, and the Jet Propulsion Laboratory/California Institute of Technology, funded by the National Aeronautics and Space Administration. This research has made use of the SVO Filter Profile Service (<http://svo2.cab.inta-csic.es/theory/fps/>) supported from the Spanish MINECO through grant AYA2017-84089.

Facilities: Keck II (NIRC2), VLT:Melipal (SPHERE).

Software: DebrisDiskFM (Ren et al. 2019), emcee (Foreman-Mackey et al. 2013), IRDAP (van Holstein et al. 2020), VIP (Gomez Gonzalez et al. 2017).

Appendix Disk-modeling Parameters

We list the best-fit parameters and their meanings in our disk models in Table 1. We have not adopted a physically motivated model to describe the observed ring, but analytically modeled the observed distribution of light assuming the disk is optically thin. Due to the unphysical nature of our disk model, we do not further discuss the physical implications of these parameters.

Table 1
Posterior Values for the HD 34282 Ring Parameters in the Keck/NIRC2 L' -Band

Parameter	Maximum Likelihood	50th \pm 34th Percentiles	Unit	Parameter Meaning
(1)	(2)	(3)	(4)	(5)
g	0.38	$0.40^{+0.05}_{-0.03}$		Forward-scattering parameter in the Henyey & Greenstein (1941) phase function.
θ_{inc}	72.3	-73^{+2}_{-2}	degree	Inclination of the ring, measured from face-on.
θ_{PA}	-74.1	$-73.8^{+1.4}_{-1.5}$	degree	Position angle of the apparent major axis of the ring, measured east of north.
r_c	140	135^{+9}_{-9}	au	Critical radius of the dust distribution for the ring model; see Equation (1).
α_{in}	2.1	6^{+8}_{-3}		Asymptotic power-law index of dust distribution for $r \ll r_c$; see Equation (1).
α_{out}	-23.1	-19^{+8}_{-8}		Asymptotic power-law index of dust distribution for $r \gg r_c$; see Equation (1).
ΔX_1	2.7	2^{+11}_{-14}	au	Ring-center offset along the disk major axis; positive is toward the southeast (Millar-Blanchaer et al. 2016).
ΔX_2	8.5	7^{+3}_{-3}	au	Ring-center offset along the disk minor axis; positive is toward disk backside (Millar-Blanchaer et al. 2016).

Note. Column 1: disk parameters of interest. Column 2: best-fit parameters used to generate the best-fit disk model. Column 3: 50th \pm 34th percentiles assuming independent pixels. Column 4: parameter units. Column 5: meaning of parameters.

ORCID iDs

Juan Quiroz  <https://orcid.org/0000-0001-8037-3779>
 Nicole L. Wallack  <https://orcid.org/0000-0003-0354-0187>
 Bin Ren (任彬)  <https://orcid.org/0000-0003-1698-9696>
 Ruobing Dong (董若冰)  <https://orcid.org/0000-0001-9290-7846>
 Jerry W. Xuan  <https://orcid.org/0000-0002-6618-1137>
 Dimitri Mawet  <https://orcid.org/0000-0002-8895-4735>
 Maxwell A. Millar-Blanchaer  <https://orcid.org/0000-0001-6205-9233>
 Garreth Ruane  <https://orcid.org/0000-0003-4769-1665>

References

- Asensio-Torres, R., Henning, T., Cantalloube, F., et al. 2021, *A&A*, 652, A101
 Augereau, J. C., Lagrange, A. M., Mouillet, D., et al. 1999, *A&A*, 348, 557
 Bae, J., Pinilla, P., & Birnstiel, T. 2018, *ApJL*, 864, L26
 Bae, J., Zhu, Z., Baruteau, C., et al. 2019, *ApJL*, 884, L41
 Baraffe, I., Chabrier, G., Barman, T. S., et al. 2003, *A&A*, 402, 701
 Biller, B. A., Males, J., Rodigas, T., et al. 2014, *ApJL*, 792, L22
 Birnstiel, T., Andrews, S. M., Pinilla, P., & Kama, M. 2015, *ApJL*, 813, L14
 Currie, T., Muto, T., Kudo, T., et al. 2014, *ApJL*, 796, L30
 de Boer, J., Ginski, C., Chauvin, G., et al. 2021, *A&A*, 649, A25
 de Boer, J., Langlois, M., van Holstein, R. G., et al. 2020, *A&A*, 633, A63
 Dong, R., & Fung, J. 2017, *ApJ*, 835, 146
 Dong, R., Hall, C., Rice, K., & Chiang, E. 2015a, *ApJL*, 812, L32
 Dong, R., Zhu, Z., Rafikov, R. R., & Stone, J. M. 2015b, *ApJL*, 809, L5
 Dong, R., Zhu, Z., & Whitney, B. 2015c, *ApJ*, 809, 93
 Flasseur, O., Thé, S., Denis, L., et al. 2021, *A&A*, 651, A62
 Foreman-Mackey, D., Hogg, D. W., Lang, D., & Goodman, J. 2013, *PASP*, 125, 306
 Gaia Collaboration, Brown, A. G. A., Vallenari, A., et al. 2021, *A&A*, 649, A1
 Gomez Gonzalez, C. A., Wertz, O., Absil, O., et al. 2017, *AJ*, 154, 7
 Haffert, S. Y., Bohn, A. J., de Boer, J., et al. 2019, *NatAs*, 3, 749
 Hall, C., Dong, R., Teague, R., et al. 2020, *ApJ*, 904, 148
 Henyey, L. G., & Greenstein, J. L. 1941, *ApJ*, 93, 70
 Husser, T. O., Wende-von Berg, S., Dreizler, S., et al. 2013, *A&A*, 553, A6
 Keppler, M., Benisty, M., Müller, A., et al. 2018, *A&A*, 617, A44
 Lodato, G., Dipierro, G., Ragusa, E., et al. 2019, *MNRAS*, 486, 453
 Maire, A. L., Stolker, T., Messina, S., et al. 2017, *A&A*, 601, A134
 Marocco, F., Eisenhardt, P. R. M., Fowler, J. W., et al. 2021, *ApJS*, 253, 8
 Marois, C., Lafrenière, D., Doyon, R., et al. 2006, *ApJ*, 641, 556
 Merín, B., Montesinos, B., Eiroa, C., et al. 2004, *A&A*, 419, 301
 Millar-Blanchaer, M. A., Graham, J. R., Pueyo, L., et al. 2015, *ApJ*, 811, 18
 Millar-Blanchaer, M. A., Wang, J. J., Kalas, P., et al. 2016, *AJ*, 152, 128
 Montesinos, M., & Cuello, N. 2018, *MNRAS*, 475, L35
 Nielsen, E. L., De Rosa, R. J., Macintosh, B., et al. 2019, *AJ*, 158, 13
 Pairet, B., Cantalloube, F., & Jacques, L. 2021, *MNRAS*, 503, 3724
 Pueyo, L. 2016, *ApJ*, 824, 117
 Quanz, S. P., Amara, A., Meyer, M. R., et al. 2013, *ApJL*, 766, L1
 Reggiani, M., Quanz, S. P., Meyer, M. R., et al. 2014, *ApJL*, 792, L23
 Ren, B., Choquet, É., Perrin, M. D., et al. 2019, *ApJ*, 882, 64
 Ren, B., Choquet, É., Perrin, M. D., et al. 2021, *ApJ*, 914, 95
 Ren, B., Pueyo, L., Chen, C., et al. 2020, *ApJ*, 892, 74
 Rodrigo, C., & Solano, E. 2020, in Scientific Meeting (virtual) of the Spanish Astronomical Society, The SVO Filter Profile Service, XIV.0 (Barcelona: SEA), 182, <https://www.sea-astronomia.es/reunion-cientifica-2020>
 Rodrigo, C., Solano, E., & Bayo, A. 2012, SVO Filter Profile Service Version 1.0, IVO Working Draft 15 October 2012
 Rosotti, G. P., Benisty, M., Juhász, A., et al. 2020, *MNRAS*, 491, 1335
 Ruane, G., Ngo, H., Mawet, D., et al. 2019, *AJ*, 157, 118
 Soummer, R., Pueyo, L., & Larkin, J. 2012, *ApJL*, 755, L28
 van der Marel, N., Williams, J. P., & Bruderer, S. 2018, *ApJL*, 867, L14
 van der Plas, G., Ménard, F., Canovas, H., et al. 2017, *A&A*, 607, A55
 van Holstein, R. G., Girard, J. H., de Boer, J., et al. 2020, *A&A*, 633, A64
 Vigan, A., Fontanive, C., Meyer, M., et al. 2021, *A&A*, 651, A72
 Villenave, M., Benisty, M., Dent, W. R. F., et al. 2019, *A&A*, 624, A7
 Wang, J. J., Ginzburg, S., Ren, B., et al. 2020, *AJ*, 159, 263
 Wolff, S. G., Perrin, M. D., Stapelfeldt, K., et al. 2017, *ApJ*, 851, 56
 Xuan, W. J., Mawet, D., Ngo, H., et al. 2018, *AJ*, 156, 156
 Zhang, S., Zhu, Z., Huang, J., et al. 2018, *ApJL*, 869, L47